Fast Theoretical Predictions for Spherical Fourier Analysis of Large-Scale Structures

Brandon Khek

Rice University, Houston, TX, 77005, USA

Henry Grasshorn Gebhardt and Olivier Doré

Jet Propulsion Laboratory, California Institute of Technology, Pasadena, CA 91109, USA and
California Institute of Technology, Pasadena, CA 91125, USA

On-going or soon to come cosmological large-scale structure surveys such as DESI, SPHEREx, Euclid, or the High-Latitude Spectroscopic Survey of the Nancy Grace Roman Space Telescope promise unprecedented measurement of the clustering of galaxies on large scales. When quantified with the Cartesian Fourier basis, the measurement of these large scales requires the introduction of so-called wide-angle corrections. By contrast, the measurement of the power spectrum in a spherical Fourier Bessel (SFB) basis does not require such corrections and naturally accounts for the spherical survey geometries. Here, we develop and implement a fast code to construct the SFB power spectrum and investigate how line of sight effects, physics such as non-Gaussianity, and differing survey geometries affect SFB power spectrum estimates. We then leverage our program to predict the tightness of cosmic growth constraints from realistic survey specifications using a Fisher matrix formalism.

I. INTRODUCTION

In order to answer questions about elusive cosmological phenomena such as dark energy and inflation, next-generation deep, wide-angle galaxy redshift surveys such as SPHEREx [1], Euclid [2], DESI [3], and Roman [4] will be launched within the next decade and will obtain spectra of hundreds of millions of galaxies. This will enable the analysis of the large-scale distribution of matter throughout space, and as a consequence, precise estimates of the cosmological parameters that govern the evolution of the universe.

The three-dimensional map of the distribution of galaxies and galaxy clusters can be studied using statistics such as the two-point correlation function which describes the probability of observing two galaxies separated by some fixed distance. However, for separation of scales, in this paper we use the power spectrum, the two-point correlation function in harmonic space. A primary advantage to this approach is that in a homogeneous and isotropic universe, the Fourier modes that comprise the power spectrum have the desirable property of being statistically orthogonal [5]. Trade-offs between the two-point function in configuration space and the power spectrum are further detailed in Feldman *et al.* [6].

Previous measurements of the 3D power spectrum have relied on Cartesian Fourier decomposition and have been sufficient for surveys with small volumes and minimal sky coverage. The Cartesian global-plane parallel power spectrum uses a single global line of sight (LOS), though this assumption becomes invalid for galaxies with large angular separations expected in upcoming wide-angle surveys. Resolutions include the local plane-parallel approximation, which uses a single LOS per galaxy pair [7] and usually involves perturbative wide-angle corrections [8, 9]. Still, these approximations break down with the full-sky coverage to be seen in next-generation surveys, resulting in a loss of information. The mismatch of the Cartesian basis and the inherent spherical geometry of the survey ultimately dictates that $P(\mathbf{k})$ is not directly measurable due to wide angle effects [10]. While large angular scales pose many challenges, large radial scales also present difficulties in a Cartesian basis. For example, the survey volume is divided into redshift bins, and the power spectrum estimator is measured at the effective redshift in each bin. Radial bins that are too large inadequately capture redshift evolution while narrow bins fail to measure radial modes larger than the bin size [10].

A spherical Fourier Bessel (SFB) decomposition of the matter overdensity field improves upon the Cartesian power spectrum with these limitations in mind. The basis functions of the SFB decomposition are defined as the eigenfunctions of the Laplacian in spherical coordinates: spherical Bessel functions and spherical harmonics for the radial and angular components of the Laplacian operator, respectively. In the SFB basis, a LOS for each galaxy is implicit, avoiding the need for flat-sky approximations, and we reduce our primary assumption to modeling redshift space distortions (RSD) to linear order [11]. Furthermore, radial distortions are naturally included in analysis and preserve isotropy, therefore maintaining statistical orthogonality of the angular modes in the real space power spectrum [12].

In this paper we develop code that computes the theoretical SFB power spectrum, tunable to survey parameters such as the selection function and survey radius, as well as different cosmologies and physical parameters like galaxy bias. We use the code to study physical effects in the power spectrum – including non-Gaussianity and RSD – and investigate the evolution of power across multipole moments. We then leverage the power spectrum estimator to predict cosmological constraints with Fisher forecasts.

In Section II, we provide a short review of the SFB decomposition formalism along with the features obtained from various physical effects and survey parameters con-

sidered in our modeling. In Section III, for this specific survey, we predict constraints on the parameters $f\sigma_8$, $b\sigma_8$, h, Ω_m, and $f_{\rm NL}$. We then conclude in Section IV. Our strategy for numerical integration is outlined in Appendix A, and we derive an approximation used in our integration for improved computational efficiency in Appendix B. Unless otherwise stated, we will use the *Planck* ΛCDM cosmological model (2018) throughout this work.

II. SFB POWER SPECTRUM

In this section, we will review the mathematical formalism of the SFB decomposition and demonstrate how physical effects, in particular evolution along the light cone, redshift space distortions (RSD), and non-Gaussianity affect the shape and amplitude of the SFB power spectrum. We also investigate how finite survey volumes contribute to changes in the width of the power spectrum. This section concludes with a discussion of the shot noise computation we use in our analyses. As an example, in this work, we consider an all-sky survey with an observed comoving number density and galaxy bias corresponding to one of the SPHEREx redshift accuracy bins, i.e. $\sigma(z)/(1+z) = 0.003$ [13, 14][15]. Note that we only consider one redshift accuracy sample out of the five expected. Because we do not implement any multi-tracer technique nor take into account redshift errors, our results do not constitute a SPHEREx forecast.

A radial survey range of z $\in [0.0, 4.6]$ with 1000 radial bins is assumed, and the linear matter power spectrum used in our computations was generated in Python using `CAMB` [16]. We will use these parameters for power spectrum estimates throughout the rest of this work unless otherwise noted. Finally, we only consider a spherically symmetric galaxy survey and leave a separate treatment of the angular mask for future work.

Continuous SFB Power Spectrum. The continuous real space and SFB modes are defined by

$$\delta(\boldsymbol{r}) = \int dk \sum_{\ell m} \sqrt{\frac{2}{\pi}} k \, j_\ell(kr) Y_{\ell m}(\theta,\,\phi)\,\delta_{\ell m}(k)\,, \quad (1)$$

$$\delta_{\ell m}(k) = \int d^3 r \left[\sqrt{\frac{2}{\pi}} k \, j_\ell(kr) Y_{\ell m}^*(\theta,\,\phi) \right] \delta(\boldsymbol{r})\,. \quad (2)$$

Following [17], we define an integral kernel

$$\mathcal{W}_\ell(k, q) = \frac{2qk}{\pi} \int dr\, \phi(r) D(r) b(r, q) j_\ell(kr) \quad (3)$$
$$\times \sum_{\Delta\ell} (\delta^K_{\Delta\ell, 0} - \beta f^\ell_{\Delta\ell}) j_{\ell+\Delta\ell}(qr)\, r^2$$

for radial selection function $\phi(r)$, linear growth factor $D(r)$, RSD parameter $\beta = f/b$, and potentially scale-dependent galaxy bias $b(r, q)$. The sum encodes the linear

RSD contribution [18], and the only non-zero $f^\ell_{\Delta\ell}$

$$f^\ell_{-2} = \frac{\ell(\ell-1)}{(2\ell-1)(2\ell+1)}\,, \quad (4)$$

$$f^\ell_0 = -\frac{2\ell^2 + 2\ell - 1}{(2\ell-1)(2\ell+3)}\,, \quad (5)$$

$$f^\ell_2 = \frac{(\ell+1)(\ell+2)}{(2\ell+1)(2\ell+3)}\,, \quad (6)$$

arise from a recursion relation of the second derivative of the spherical Bessel function. We have omitted the "fingers-of-God" effect because of its negligible contribution on the larger scales ($k_{n\ell} < 0.15\,h\,{\rm Mpc}^{-1}$) studied in this paper. The definition of the integral kernel serves to concisely write the redshift-space, i.e. observed, galaxy density contrast to linear order in the SFB basis $\delta^{\rm obs}_{\ell m}(k)$,

$$\delta^{\rm obs}_{\ell m}(k) = \int dq\, \mathcal{W}_\ell(k, q)\, \delta_{\ell m}(q)\,, \quad (7)$$

whereas $\delta_{\ell m}(q)$ denotes the density contrast of the matter field only. We can then write the continuous SFB power spectrum as

$$C_\ell(k, k') \equiv \langle \delta^{\rm obs}_{\ell m}(k)\, \delta^{{\rm obs},*}_{\ell m}(k') \rangle \quad (8)$$
$$= \int dq\, \mathcal{W}_\ell(k, q) \mathcal{W}^*_\ell(k', q) P(q)\,.$$

Discretized SFB Power Spectrum. Boundary conditions must be imposed on the matter overdensity field in order to maintain orthogonality of the spherical Laplacian eigenfunctions under the consideration of a finite survey radius from $r_{\rm min}$ to $r_{\rm max}$, resulting in a discretization of the SFB modes [19].

The discretized real space and SFB pair are defined by

$$\delta(\boldsymbol{r}) = \sum_{n\ell m} [g_{n\ell}(r) Y_{\ell m}(\theta,\,\phi)]\,\delta_{n\ell m}, \quad (9)$$

$$\delta_{n\ell m} = \int \int_{r_{\rm min}}^{r_{\rm max}} r^2\, dr\, d\Omega\, g_{n\ell}(r)\, Y^*_{\ell m}(\theta,\,\phi)\,\delta(\boldsymbol{r})\,, \quad (10)$$

where $g_{n\ell}$ is a linear combination of spherical Bessel functions of the first and second kind

$$g_{n\ell}(r) = c_{n\ell}\, j_\ell(k_{n\ell}\, r) + d_{n\ell}\, y_\ell(k_{n\ell}\, r) \quad (11)$$

at discrete radial scales $k_{n\ell}$. The $g_{n\ell}$ serve as eigenfunctions to the radial component of the Laplacian under potential boundary conditions with eigenvalues $-k^2_{n\ell}$, and in practice they are computed using the code `SphericalFourierBesselDecompositions.jl` [17].

Substituting Eq. (1) with the observed density contrast into Eq. (10), we exploit the orthogonality relation of spherical harmonics to obtain the relation between the continuous and discrete SFB-space density contrasts,

$$\delta^{\rm obs}_{n\ell m} = \int \left[\int_{r_{\rm min}}^{r_{\rm max}} g_{n\ell}(r) \sqrt{\frac{2}{\pi}} k\, j_\ell(kr)\, r^2\, dr \right] \delta^{\rm obs}_{\ell m}(k)\, dk\,. \quad (12)$$
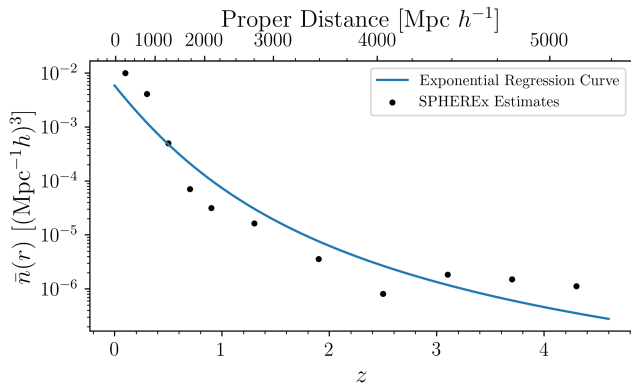
FIG. 1. Average galaxy number density data used throughout this paper. A simple exponential regression curve of the form Eq. (16) was fitted to the SPHEREx $\sigma(z)/(1+z) \leq 0.003$ sample number density estimates given in black. Reduced observations of galaxies at larger redshifts results in the decay of the selection function.

Modeling the observed density contrast as in Eqs. (3) and (7), we obtain

$$\delta_{n\ell m}^{\mathrm{obs}} = \int dq \, \mathcal{W}_{n\ell}(q) \, \delta_{\ell m}(q) \,, \tag{13}$$

where

$$\mathcal{W}_{n\ell}(q) = \sqrt{\frac{2q^2}{\pi}} \int_{r_{\min}}^{r_{\max}} g_{n\ell}(r) \, \phi(r) D(r) b(r,q) \tag{14}$$
$$\times \sum_{\Delta\ell} (\delta_{\Delta\ell,0}^K - \beta f_{\Delta\ell}^\ell) j_{\ell+\Delta\ell}(qr) \, r^2 dr \,.$$

Compared to the continuous limit Eq. (3), in the discrete case, the first spherical Bessel is substituted by the discrete basis functions $g_{n\ell}(r)$ in Eq. (14). Thus, we define the discrete SFB power spectrum assuming isotropy around the observer ($\ell = \ell'$, $m = m'$) as the covariance between observed SFB modes $\delta_{n\ell m}^{\mathrm{obs}}$, or

$$C_\ell (k_{n\ell}, k_{n'\ell}) \equiv \langle \delta_{n\ell m}^{\mathrm{obs}} \delta_{n'\ell m}^{\mathrm{obs}} \rangle$$
$$= \int \mathcal{W}_{n\ell}(q) \mathcal{W}_{n'\ell}(q) P(q) \, dq. \tag{15}$$

Obtaining this quantity in practice can be computationally intensive, therefore we employ the procedure described in Appendix B for faster calculations.

A. Radial selection function

The observed galaxy number density $\bar{n}$ is not spatially homogeneous due to inevitable magnitude limitations in galaxy surveys, resulting in more nondetections at higher redshifts. This bias toward galaxies proximal to the survey's minimum radius can be expressed in the form of the selection function ϕ. A plot of the estimated SPHEREx average galaxy number density with forecasted $\sigma(z)/(1+z) \leq 0.003$ is given in Fig. 1, and we use an exponential regression model fitted to this number density to model the selection function as

$$\bar{n}(r) = \bar{n}_0 \exp\{-r/r_0\} \tag{16}$$

where $\bar{n}_0 \approx 0.005876 \ (h/\mathrm{Mpc})^3$ and $r_0 \approx 526.2 \ \mathrm{Mpc}/h$. We define the selection function as $\phi(r) = \bar{n}(r)/\bar{n}_0$ where the normalization $\bar{n}_0$ is the maximum value attained by $\bar{n}(r)$.

In a homogeneous and isotropic universe, complete delocalization of the matter overdensity field results in a completely localized Fourier transform with power only along the diagonal $k_{n\ell} = k_{n'\ell}$. In this case, the SFB modes, and therefore clustering at scales $k_{n\ell}$ and $k_{n'\ell}$, are uncorrelated. However, inhomogeneity on the light cone breaks this symmetry. In Fig. 2, we compare the effects of a constant and exponential selection function on the SFB power spectrum. The latter results in more power for off-diagonal terms $k_{n\ell} \neq k_{n'\ell}$ than the former due to an observed radial inhomogeneity as the observed galaxy number density decreases at farther distances. The correlation between SFB modes is a result of the broken translational invariance in the real-space overdensity field. In other words, following the uncertainty principle, the lack of homogeneity in real space no longer results in a SFB transform with power at a single $k_{n\ell}$ frequency, but instead we obtain coupled SFB coefficients. Furthermore, a finite survey volume limits the number of basis functions in the effective volume which prevents statistical orthogonality among the SFB coefficients.

B. Redshift-space distortions

Peculiar velocities and cosmological expansion biases estimates of distances to galaxies that use redshifts. In particular, in large-scale structures, the infall of galaxies toward the a common gravitational center results in a redshift of light emitted from galaxies infalling along the LOS direction and blueshift of those antiparallel to it. This LOS effect, known as the Kaiser effect, results in inferences of more clustering on large scales than is present in real space. A consequence of RSD is therefore an increase in the clustering amplitude of the power spectrum on large scales, as shown in Fig. 3. While the power is increased for terms adjacent and parallel to the diagonal, the width of the diagonal itself remains relatively unchanged. The slight shift of the SFB power spectrum amplitude to larger $k_{n\ell}$ with RSD can be attributed to the "squashing" of large-scale structures to smaller scales from the LOS component of the galaxies' peculiar velocities.

We can also observe where the power resides as a function of ℓ for fixed k and k'. In Fig. 4, the SFB power spectrum is shown for $\ell = 2, \ldots, 75$ in redshift space with the exponential selection function. Small ℓ probes larger angular scales, resulting in more power at small k and k' which decreases rapidly as ℓ increases. Conversely, larger
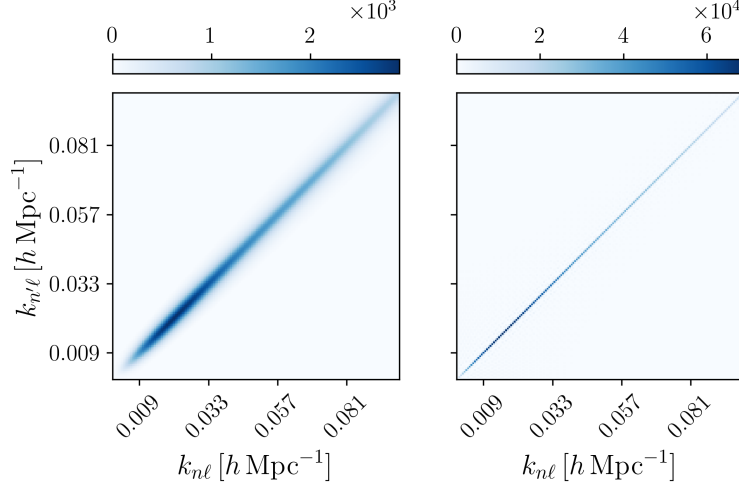
FIG. 2. SFB power spectrum $C_\ell(k_{n\ell}, k_{n'\ell})$ in $\left[h^{-1}\text{Mpc}\right]^4$ for $\ell = 2$ with Left: SPHEREx-based exponential radial selection function. Right: Constant selection function $\phi(r) = 1$.
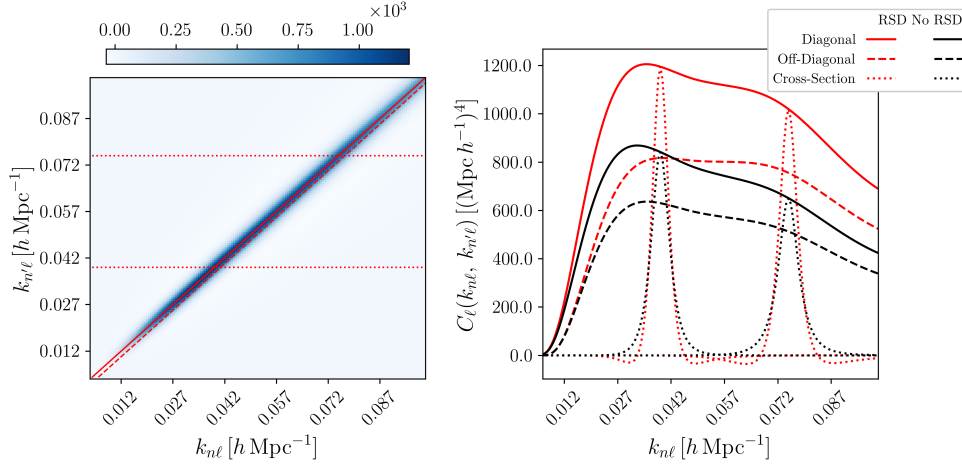

FIG. 3. SFB power spectrum for $\ell = 10$ with and without RSD. Left: Heatmap of the SFB power spectrum with RSD included. One-dimensional cuts are highlighted in red and displayed in the right plot. The same cuts are taken from the SFB power spectrum without RSD. Right: One-dimensional cuts of the SFB power spectrum. Red lines are slices of the SFB power spectrum in redshift space, and black is without RSD. Solid lines are diagonal cuts, dashed lines indicate off-diagonal cuts, and dotted lines are cross-sections.

ℓ, or smaller angular scales, finds more power in smaller radial scales, hence higher k and k'. The lines of constant slope can be explained by applying Limber's approximiation Eq. (B1) to Eq. (15). The exponential selection function dominates the decay rate, resulting in straight lines. The magnitude of the slopes for different k is also explained by the argument to the selection function in this approximation. Additionally, we observe the typical $k = k'$ values where the power lies as a function of ℓ, shown in Fig. 5. Here, we have used a weighted average of each $k_{n\ell}$ mode based on the power at that scale for a fixed ℓ. Again, we observe that the characteristic sizes of matter overdensities shift to smaller scales as the angular scales decrease, as expected.

C. Non-Gaussianity

The slow-roll, single-field inflationary paradigm predicts a mostly Gaussian random density field [20]. Constraining the level of non-Gaussianity (NG) of matter overdensities serves in delineating which inflationary models best describe the complex physical processes of the early universe. In some of these models, NG can be captured by the SFB power spectrum as an observable on large scales. This is due to the fact that large-scale structure falls on the tail of the probability distribution of the real space density contrast, making it especially sensitive to the skewness resulting from NG [21].
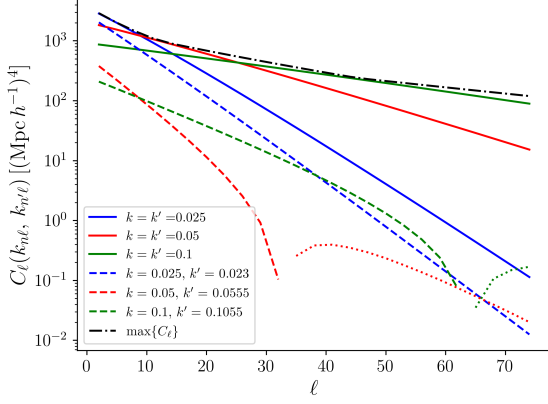
FIG. 4. The SFB power spectrum at a fixed k and k' with varying ℓ. Lines of constant slope appear due to the dominating decay rate of the exponential selection function. The power spectrum becomes negative on the off-diagonal, so the absolute value of the power is displayed as the dotted lines.
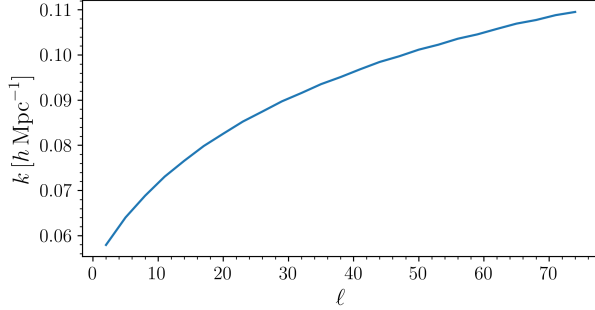

FIG. 5. $k = k'$ value at which the clustering amplitude is typically the largest for a fixed ℓ. We use a weighted average based on the power at each $k_{n\ell}$ to determine the k.

We adopt a galaxy bias with a scale-dependent correction term

$$\Delta b(r, k) = 2(b-1)f_{\mathrm{NL}}\delta_c \frac{3\Omega_m}{2\widetilde{D}(r)T(k)r_H^2 k^2} \quad (17)$$

as given in Dalal $et\ al.$ [21] and Zhang $et\ al.$ [22] to measure the SFB power spectrum under the assumption of primordial non-Gaussianity. Here, b is the fiducial galaxy bias, $T(k)$ is the matter transfer function, $\widetilde{D}(r)$ is the growth factor normalized to the scale factor during matter domination, r_H is the Hubble radius, f_{NL} characterizes the dependence of the amplitude on non-Gaussian effects, and we take the critical overdensity as $\delta_c = 1.686$.

Fig. 6 displays how NG is realized in the SFB PS. In the plot, f_{NL} is exaggerated from typically constrained values [23] for demonstration. The power spectrum amplitude is increased at very large scales $k_{n\ell} \lesssim 0.05h\ \mathrm{Mpc}^{-1}$. This scaling is maximized along the diagonal, and off-diagonal terms do not see as large of an increase in power. The width of the diagonal shows no discernible change with

nonzero f_{NL}. Most of the information to be extracted from the SFB power spectrum with regard to NG lies at small $k = k'$ and ℓ values.

D. Shot Noise

Studying the overdensity field in the cosmic variance-limited case is instructive for isolating and exploring the manifestations of physical effects in the SFB power spectrum. However, in order to perform meaningful statistical analyses, we must account for shot noise, which increases the uncertainty in measurements of quantities such as the cosmological parameters due to the sampling of finitely many galaxies within the survey volume. From [17], the shot noise matrix elements are given via

$$N_{\ell n n'}^{\mathrm{obs}} = \frac{1}{n_0}\frac{1}{\sqrt{4\pi}}\int dr\,r^2\,g_{n\ell}(r)\,g_{n'\ell}(r)\,W_{00}(r)\,, \quad (18)$$

where, assuming that the full window W_{00} is separable into a mask $M(\hat{\mathbf{r}})$ and radial selection $\phi(r)$,

$$W_{00}(r) = \int d\Omega\,Y_{00}^*(\theta, \varphi)\,M(\theta, \varphi)\,\phi(r) \quad (19)$$

$$\simeq \sqrt{4\pi}\,\phi(r)\,f_{\mathrm{sky}}\,, \quad (20)$$

for fractional sky coverage f_{sky}. Thus,

$$N_{\ell n n'}^{\mathrm{obs}} = \frac{f_{\mathrm{sky}}}{n_0}\int dr\,r^2\,g_{n\ell}(r)\,g_{n'\ell}(r)\,\phi(r), \quad (21)$$

where n_0 is the maximum galaxy number density within the survey. The shot noise matrix is then simply added to the power spectra. In this work, the window function consists only of the radial selection function, and we approximate the fractional sky coverage after calculating the Fisher information as shown in the next section, thereby setting $f_{\mathrm{sky}} = 1$ in Eq. (21) to avoid accounting for the angular selection function twice. We leave a more precise treatment of the angular mask for future work. For demonstration, $N_{\ell n n'}^{\mathrm{obs}}$ for $\ell = 2$ is displayed in Fig. 7. The shot noise dominates at smaller scales where it asymptotes to a constant. This can be explained by the fact that in Eq. (21), the $g_{n\ell}$ remain approximately zero until peaking around $r = (\ell + 1/2)/k_{n\ell}$, which is found using the Limber approximation described in Appendix B in the case that $r_{\min} \approx 0$. Thus, increasing $k_{n\ell}$ shifts the peak so that oscillations begin to enter the survey boundary and contribute to the integral.

III. FISHER MATRIX FORECASTING

We will now leverage our code to predict the considered survey constraints on cosmological parameters $\boldsymbol{\theta} = (h, \Omega_m, f_{\mathrm{NL}}, f\sigma_8, b\sigma_8)$. We review the Fisher forecasting formalism before presenting our results.
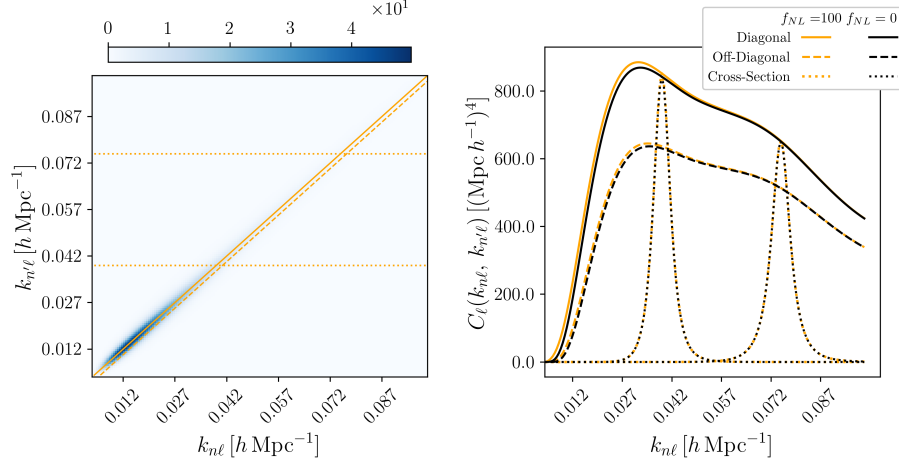
FIG. 6. SFB power spectrum in real space for $\ell = 10$ with and without non-Gausianity. Left: Difference between the SFB power spectrum with $f_{\mathrm{NL}} = 100$ and with $f_{\mathrm{NL}} = 0$. One-dimensional cuts are highlighted in gold and displayed in the right graph with the undifferenced power spectra. Right: One-dimensional cuts of the SFB power spectrum. Gold lines are slices with $f_{\mathrm{NL}} = 100$, and black is with $f_{\mathrm{NL}} = 0$.
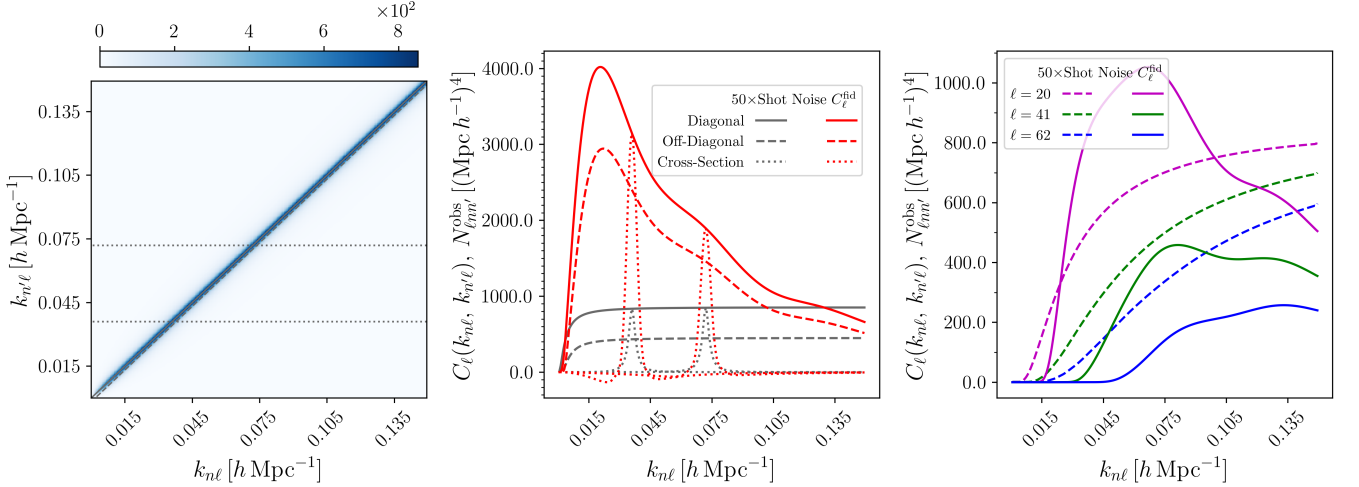

FIG. 7. Comparison of the shot noise, multiplied by a factor of 50 in each plot, and the SFB power spectrum for $\ell = 2$. Left: Shot noise matrix. One-dimensional cuts are shown in gray and displayed in the middle graph. Middle: One-dimensional cuts of the shot noise and SFB power spectrum with RSD. Gray lines are slices from the left plot, and red are the same cuts from the SFB PS. Right: Rescaled shot noise (dashed) and SFB power spectrum (solid) for larger ℓ.

We construct the likelihood function by defining the data vector in SFB space, $\hat{\boldsymbol{\delta}} \equiv \delta^{\mathrm{obs}}_{n\ell m}$. Then, the probability of measuring this data vector given parameters $\boldsymbol{\theta}$ is given by the Gaussian likelihood function

$$\mathcal{L}(\hat{\boldsymbol{\delta}} \,|\, \boldsymbol{\theta}) = \frac{1}{(2\pi)^{\dim(\hat{\boldsymbol{\delta}})/2}\sqrt{|\mathcal{C}|}} \exp\left\{-\frac{1}{2}\hat{\boldsymbol{\delta}}\,\mathcal{C}^{-1}\hat{\boldsymbol{\delta}}\right\}, \quad (22)$$

where $\mathcal{C} \equiv C_\ell(k_{n\ell}, k_{n'\ell}) + N^{\mathrm{obs}}_{\ell nn'}$ is the discretized SFB power spectrum with shot noise Eq. (21). We denote θ_n as the nth parameter in $\boldsymbol{\theta}$ and define $\square_{,\alpha} \equiv \partial\square/\partial\theta_\alpha$. Then, the Fisher matrix element at indices α and β is

given by

$$F_{\alpha\beta} = \left\langle -(\ln \mathcal{L})_{,\alpha\beta} \right\rangle. \quad (23)$$

which, through Eq. (22), can be rewritten as

$$F_{\alpha\beta} = f_{\mathrm{sky}} \sum_{\ell=\ell_{\min}}^{\ell_{\max}} \frac{2\ell+1}{2} \mathrm{tr}\left(\mathcal{C}^{-1}\mathcal{C}_{,\alpha}\mathcal{C}^{-1}\mathcal{C}_{,\beta}\right), \quad (24)$$

given a fractional sky coverage f_{sky} and $2\ell+1$ m-modes per ℓ. Here, we choose $\ell_{\min} = 2$ to avoid systematics associated with the monopole and dipole contributions, such as our own peculiar velocity. Additionally, we choose

$\ell_{\max}$ *a posteriori* with observation of when the $\ell \approx \ell_{\max}$ mode contributions to the reduction of errors on $\boldsymbol{\theta}$ become negligible, as will be later shown in Fig. 10. Finally, the covariance matrix of the parameters $\boldsymbol{\theta}$ is obtained via the inversion of the Fisher information matrix

$$C_{\alpha\beta} = (F^{-1})_{\alpha\beta}. \tag{25}$$

Derivatives of the power spectra are computed numerically by inducing small perturbations in the cosmological parameters $\alpha, \beta \in \boldsymbol{\theta}$, then dividing the differenced fiducial and perturbed power spectra by the perturbation size. This is straightforward for h, Ω_m, and f_{NL}, though for $f\sigma_8(z)$ and $b\sigma_8(z)$, we model deviations from the reference cosmology by a low-order polynomial in redshift as described in Section III A.

In order to compute the numerical derivatives of the power spectrum with respect to parameters Ω_m and h, we must calculate the input matter power spectrum in a universe different than the *Planck* flat ΛCDM model used throughout this work. The perturbed parameters result in a different set of basis functions for the SFB decomposition and therefore different wavenumbers k. Thus, to difference SFB power spectra between cosmologies, we calculate the SFB power spectrum in the perturbed cosmological model, perform a two-dimensional spline, and evaluate the splined SFB power spectrum at the allowed wavenumbers in the fiducial cosmology.

A. Modeling the Redshift Evolution

Here, we describe the model used for $f\sigma_8$ and $b\sigma_8$ in our Fisher matrix calculation. We only explicitly write the model for $f\sigma_8$ because $b\sigma_8$ has the same form, so the substitution $f\sigma_8 \leftarrow b\sigma_8$ and $f(z) \leftarrow b(z)$ can be made to obtain the equations for $b\sigma_8$.

Given a fiducial form $f\sigma_8^{\mathrm{fid}}(z) = f(z)\,D(z)\,\sigma_8$ where σ_8 is evaluated at redshift $z = 0$, we model the true functional form by a modulation with a low-order polynomial. That is,

$$f\sigma_8(z) \equiv f\sigma_8^{\mathrm{fid}}(z) \sum_{i=0}^{n} a_i z^i, \tag{26}$$

where a_i are the parameters to be fit and n is the order of the polynomial. The goal is then to obtain uncertainties for the parameters a_i from our Fisher analysis.

To obtain an uncertainty forecast for $f\sigma_8(z)$ itself, we propagate the uncertainties in the a_i to linear order. That is, we assume that small changes Δa_i will lead to a change $\Delta f\sigma_8(z)$

$$\Delta f\sigma_8(z) \approx \sum_{i=0}^{n} \frac{\partial f\sigma_8(z)}{\partial a_i}\,\Delta a_i. \tag{27}$$

The variance in $f\sigma_8(z)$ is then given by

$$\langle (\Delta f\sigma_8)^2 \rangle = \sum_{ij} A_{ij}\,\langle \Delta a_i\,\Delta a_j \rangle, \tag{28}$$
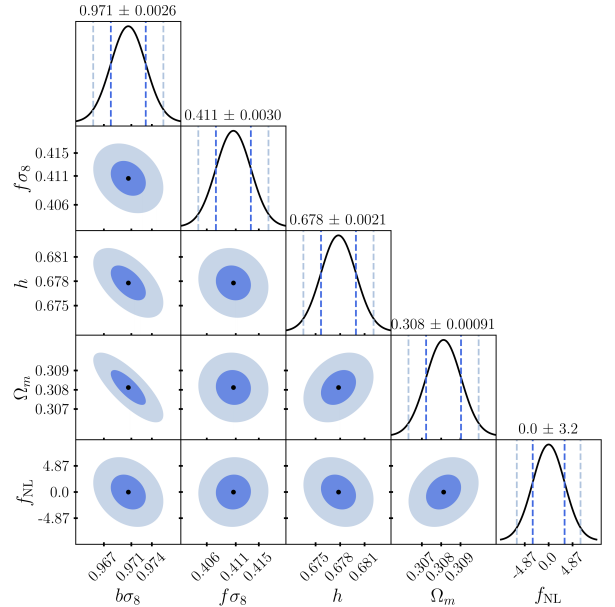

FIG. 8. Forecasted constraints on cosmological parameters at $z = 0$ in a survey from $z = 0$ to 4.6 with $k_{\max} = 0.15\,h/\mathrm{Mpc}$ and $\ell = 2, \ldots, 224$ and 80% sky coverage. We truncate uncertainties to two significant digits in the interest of space, though more precise values are given in the text. Dark blue and light blue indicate the 68% and 95% confidence level regions, respectively. For $f\sigma_8$ and $b\sigma_8$, we marginalize only over a_1 and spline the galaxy bias and selection function described above.

where the sum is over $i, j = 0, \ldots, n$ and

$$A_{ij} = \left[f\sigma_8^{\mathrm{fid}}(z) \right]^2 z^{i+j}, \tag{29}$$

where we assumed the modulated model Eq. (26). The covariance between the coefficients a_i and a_j is found from the inversion of the Fisher information matrix

$$\langle \Delta a_i\,\Delta a_j \rangle = \left(F^{-1} \right)_{ij}. \tag{30}$$

Therefore, by evaluating the Fisher information matrix, we can find the uncertainty in $f\sigma_8$ as a function of redshift.

B. Fisher Forecast Results

We present forecasts for the survey we consider in Fig. 8 where we have adopted the galaxy bias correction due to local primordial non-Gaussianity given in Eq. (17) for our estimates of f_{NL}. We have forecasted $b\sigma_8 = 0.9706 \pm 0.00255$, $f\sigma_8 = 0.4106 \pm 0.00303$, $h = 0.6778 \pm 0.00215$, $\Omega_m = 0.3081 \pm 0.000906$, and $f_{\mathrm{NL}} = 0 \pm 3.25$. The uncertainties for $b\sigma_8$ and $f\sigma_8$ are obtained by modulating the perturbative expansion of these models only to zeroth order. Furthermore, we take
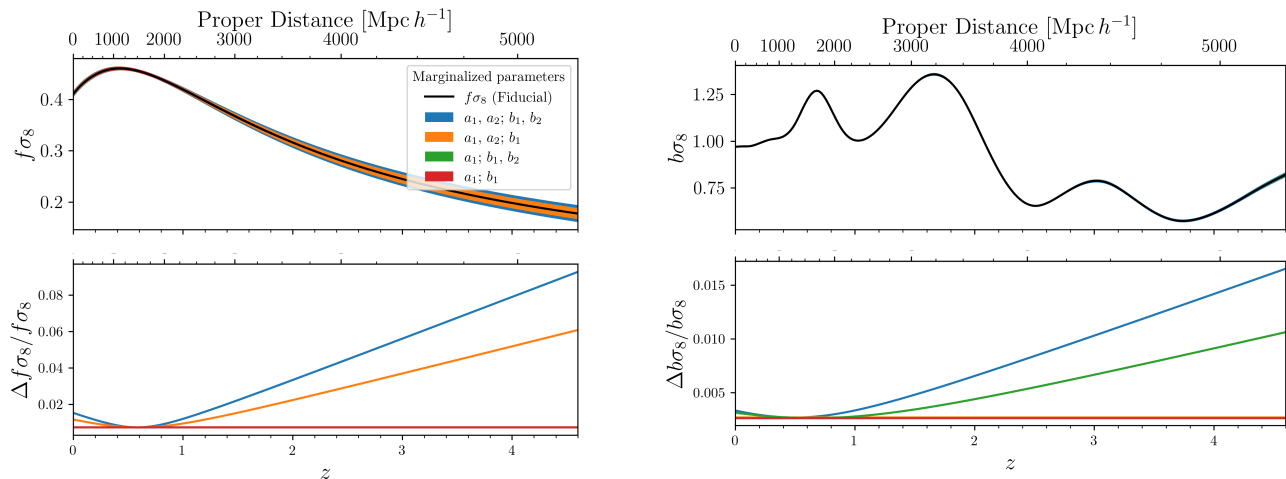
FIG. 9. Redshift evolution of $f\sigma_8$ and $b\sigma_8$ from the Fisher forecast for $\ell = 2, \ldots, 224$. The 68% confidence level band is shown as the shaded region in top panel of both plots, though is not visible for some parameters due to the small error. Thus, the normalized error is plotted alone in the bottom panels. The legend refer to coefficients in Eq. (27) for $f\sigma_8$ as a_i and as b_i for $b\sigma_8$. Left: For example, we take $a_1 = 1.01$ and $b_1 = 1.0001$ in the modulation of $f\sigma_8$ and $b\sigma_8$ from Eq. (27) for the red-shaded region. The error curve in green is approximately the same as that in red. Right: The same plot as the left, though for constraints on $b\sigma_8$. The error curve in orange is approximately the same as that in red.
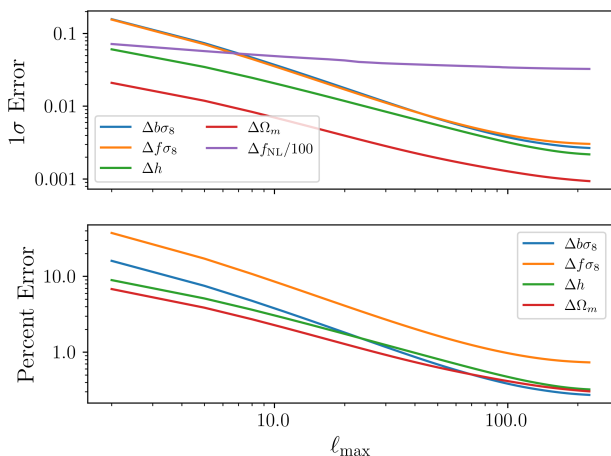

FIG. 10. Constraints on cosmological parameters as a function of the maximum ℓ mode used in the forecast, starting from $\ell = 2$, for perturbed a_1 and a_2 in $b\sigma_8$ and a_1 in $f\sigma_8$. Note that the constraint on f_{NL} has been scaled to fit the top plot.

$f_{sky} = 0.8$ and use a selection function and bias model splined from the public data described in Section II A.

Fig. 9 shows the evolution of $f\sigma_8$ and $b\sigma_8$ within the survey range with a 1σ error band from the Fisher forecast. Note that some regions are almost identical and overlap, as described in the caption. At $z \gtrsim 1$, the variance Eq. (28) scales quadratically at high z when including terms up to linear order in our polynomial expansion, thus, the standard deviation evolves linearly. Fig. 10 indicates that most of the information from our analysis

has been extracted from the power spectrum. Multipoles above $\ell = 200$ contribute negligibly to reducing error estimates. In particular, uncertainty for f_{NL} is primarily reduced at large angular scales as a result of the scale-dependent bias correction $\Delta b(r, k) \propto k^{-2}$. The imprint of non-Gaussianity on the cosmological overdensity field will primarily manifest itself in the linear regime.

IV. CONCLUSIONS

We have written code that calculates the SFB power spectrum and have leveraged our program to investigate the effects of survey geometry, RSD, and NG on the power spectrum clustering amplitude and the correlation between SFB modes. We have observed that the biased sampling of galaxies described by the selection function causes inhomogeneity on our past light cone, resulting in a correlation of terms $k_{n\ell} \neq k_{n'\ell}$ due to the real space density contrast no longer being completely delocalized. The local motion of galaxies within large-scale structure from gravitational clustering results in a LOS component of the galaxies' velocities that contributes to the observed redshift, biasing inferred distance estimates and resulting in an increase of the power spectrum amplitude in redshift space. NG, due to the sensitivity of large-scale structure to perturbations in the distribution of the real space overdensity, arises measurably on large scales. The evolution of the power spectrum as a function of multipole moment was also studied, and we showed that the typical length scale at which the clustering amplitude is largest is positively correlated with the ℓ mode in consideration.

Including shot noise and a spherically symmetric an-

gular mask with 80% sky coverage, and assuming source distributions, we forecasted uncertainties on the parameters $f\sigma_8$, $b\sigma_8$, h, Ω_m, and f_{NL} using the Fisher information matrix formalism. We have also obtained the uncertainties on $f\sigma_8$ and $b\sigma_8$ as a function of redshift, and by evaluating the contribution of higher multipoles to the constraints, we have verified that information has been maximally extracted from the power spectrum estimator.

Appendix A: Gauss-Legendre Quadrature

The Gauss-Legendre quadrature integration algorithm is crucial in our optimization of our code. The integral approximation takes the form of

$$\int_{-1}^{1} f(x)dx \approx \sum_{i=1}^{n} w_i f(x_i) \tag{A1}$$

for nodes x_i and weights w_i. We utilize the Julia module `FastGaussQuadrature.jl` [24] to calculate the nodes and weights. This approximation is used to compute the integral kernel $\mathcal{W}_{n\ell}$. The integral defining the kernel has integration bounds $r_{\min}$ and $r_{\max}$, thus, we perform a change of variables to obtain the form of Eq. (A1),

$$\int_{a}^{b} f(x)\,dx = \frac{b-a}{2} \int_{-1}^{1} f\left(\frac{b-a}{2}u + \frac{b+a}{2}\right)\,du. \tag{A2}$$

The same change of variables is performed with the SFB power spectrum in Eq. (15) over the total integration region described in Appendix B.

Appendix B: Width Estimate of $\mathbf{W}_{n\ell}(\mathbf{k}, \mathbf{q})$

Because the SFB power spectrum $C_\ell(k_{n\ell}, k_{n'\ell})$ is defined by an integral over the kernels $W_{n\ell}(q)$ as given in Eq. (15), we find the bounds of integration that allow us to approximate the integral without having to evaluate it over the entire positive real line. We take advantage of the fact that the kernels have a single sharp peak and attain a value of about zero outside of the region of the maximum. Here we derive a width estimate - akin to the equivalent widths used in spectroscopy - of these kernels.

The Limber-like approximation [25, 26] can be distilled down to a substitution

$$j_\ell(kr) \approx \sqrt{\frac{\pi}{2kr}} \delta^D\left(kr - \ell - \frac{1}{2}\right). \tag{B1}$$

Clearly, in general this is a poor approximation. However, our goal here is to obtain a rough estimate for the range of q-values over which the $\mathcal{W}_{n\ell}(q)$ kernel does not effectively vanish. We apply this in Eq. (3), obtaining

$$\mathcal{W}_\ell(k,q) \approx \sqrt{kq} \int dr\, r\, \phi(r)\, D(r)\, b(r,q)\delta^D\left(kr - \ell - \frac{1}{2}\right)$$
$$\times \sum_{\Delta\ell}(\delta^K_{\Delta\ell,0} - \beta f^\ell_{\Delta\ell})\delta^D\left(qr - \ell - \Delta\ell - \frac{1}{2}\right), \tag{B2}$$

which is only nonzero for $r = \frac{\ell+1/2}{k}$. Substituting for r, multiplying by $\sqrt{k}/\sqrt{k}$, and factoring $\frac{\ell+1/2}{k}$ from the delta function inside the sum yields

$$\mathcal{W}_\ell(k,q) \approx \sqrt{\frac{q}{k}}\, \phi\left(\frac{\ell+\frac{1}{2}}{k}\right) D\left(\frac{\ell+\frac{1}{2}}{k}\right) b\left(\frac{\ell+\frac{1}{2}}{k}, q\right)$$
$$\times \sum_{\Delta\ell}(\delta^K_{\Delta\ell,0} - \beta f^\ell_{\Delta\ell})\delta^D\left(q - \frac{\ell+\Delta\ell+\frac{1}{2}}{\ell+\frac{1}{2}}k\right). \tag{B3}$$

For $\Delta\ell \ll \ell$, we require $k \approx q$, so the delta function in the sum effectively becomes $\delta^D(q - k)$. Integration over the kernel is only nonzero for $k = q$, thus

$$\int_0^\infty W_\ell(k,q)\,dq \approx \phi\left(\frac{\ell+\frac{1}{2}}{k}\right) D\left(\frac{\ell+\frac{1}{2}}{k}\right) \tag{B4}$$
$$\times b\left(\frac{\ell+\frac{1}{2}}{k}, q\right) \sum_{\Delta\ell}(\delta^K_{\Delta\ell,0} - \beta f^\ell_{\Delta\ell}),$$

which is easily computed, and the width estimate, which we term the *equivalent width* w of the kernel, is given by

$$w = \frac{\int_0^\infty W_\ell(k,q)\,dq}{W_\ell(k,k)}, \tag{B5}$$

with the assumption that the maximum of $W_\ell(k,q)$ occurs when $k = q$. The results of this calculation is shown in Fig. 11. In practice, we spline each $\mathcal{W}_{n\ell}$ using points sampled finely in the interval around $k = q$; the interval's size is proportional to the equivalent width. Outside of the interval, we sample less finely. This allows us to accurately capture the concavity of the function and maintain accuracy for off-diagonal terms. The splined kernel is then used in the SFB power spectrum calculations.
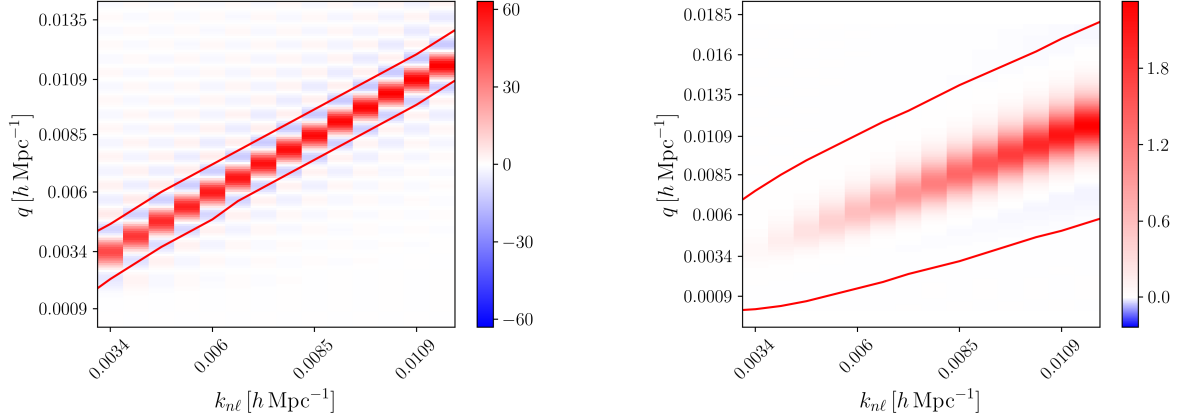
FIG. 11. Left: Equivalent width estimate of the integral kernels $W_{n\ell}(q)$ $\left[h^{-1} \, \mathrm{Mpc} \right]$ for $\ell = 10$ with a constant selection function. Two equivalent widths are used as the finely sampled region, displayed in red, centered around the peak of the kernel. While our calculation was formed on the assumption that $\Delta\ell \ll \ell$, the equivalent width estimation still performs well without satisfying this condition. Right: The same plot, though with the SPHEREx exponential selection function described in Section II A. Here, oscillations off of the diagonal are heavily suppressed.

[1] https://spherex.caltech.edu/.
[2] https://www.euclid-ec.org/.
[3] DESI Collaboration, The DESI Experiment Part I: Science,Targeting, and Survey Design, arXiv e-prints , arXiv:1611.00036 (2016), arXiv:1611.00036 [astro-ph.IM].
[4] https://roman.gsfc.nasa.gov/.
[5] A. J. S. Hamilton, Linear redshift distortions: A review, in *The Evolving Universe: Selected Topics on Large-Scale Structure and on the Properties of Galaxies*, edited by D. Hamilton (Springer Netherlands, Dordrecht, 1998) pp. 185–275.
[6] H. A. Feldman, N. Kaiser, and J. A. Peacock, Power-Spectrum Analysis of Three-dimensional Redshift Surveys, ApJ **426**, 23 (1994), arXiv:astro-ph/9304022 [astro-ph].
[7] K. Yamamoto, M. Nakamichi, A. Kamino, B. A. Bassett, and H. Nishioka, A Measurement of the Quadrupole Power Spectrum in the Clustering of the 2dF QSO Survey, Publications of the Astronomical Society of Japan **58**, 93 (2006), https://academic.oup.com/pasj/article-pdf/58/1/93/23993271/pasj58-0093.pdf.
[8] E. Castorina and M. White, Beyond the plane-parallel approximation for redshift surveys, MNRAS **476**, 4403 (2018), arXiv:1709.09730 [astro-ph.CO].
[9] F. Beutler, E. Castorina, and P. Zhang, Interpreting measurements of the anisotropic galaxy power spectrum, J. Cosmology Astropart. Phys. **2019**, 040 (2019), arXiv:1810.05051 [astro-ph.CO].
[10] M. Wang, S. Avila, D. Bianchi, R. Crittenden, and W. Percival, Hybrid-basis inference for large-scale galaxy clustering: combining spherical and cartesian fourier analyses, Journal of Cosmology and Astroparticle Physics **2020** (10), 022.
[11] A. F. Heavens and A. N. Taylor, A Spherical Harmonic Analysis of Redshift Space, Mon. Not. Roy. Astron. Soc. **275**, 483 (1995), arXiv:astro-ph/9409027.
[12] K. B. Fisher, C. A. Scharf, and O. Lahav, A spherical harmonic approach to redshift distortion and a measurement of Omega(0) from the 1.2-Jy IRAS Redshift Survey, MNRAS **266**, 219 (1994), arXiv:astro-ph/9309027 [astro-ph].
[13] O. Doré, J. Bock, M. Ashby, P. Capak, A. Cooray, R. de Putter, T. Eifler, N. Flagey, Y. Gong, S. Habib, K. Heitmann, C. Hirata, W.-S. Jeong, R. Katti, P. Korngut, E. Krause, D.-H. Lee, D. Masters, P. Mauskopf, G. Melnick, B. Mennesson, H. Nguyen, K. Öberg, A. Pullen, A. Raccanelli, R. Smith, Y.-S. Song, V. Tolls, S. Unwin, T. Venumadhav, M. Viero, M. Werner, and M. Zemcov, Cosmology with the SPHEREX All-Sky Spectral Survey, arXiv e-prints , arXiv:1412.4872 (2014), arXiv:1412.4872 [astro-ph.CO].
[14] N. R. Stickley, P. Capak, D. Masters, R. de Putter, O. Doré, and J. Bock, An Empirical Approach to Cosmological Galaxy Survey Simulation: Application to SPHEREx Low-Resolution Spectroscopy, arXiv e-prints , arXiv:1606.06374 (2016), arXiv:1606.06374 [astro-ph.IM].
[15] https://github.com/SPHEREx/Public-products.
[16] https://camb.readthedocs.io/en/latest/.
[17] H. S. Grasshorn Gebhardt and O. Doré, Fabulous code for spherical Fourier-Bessel decomposition, Phys. Rev. D **104**, 123548 (2021), arXiv:2102.10079 [astro-ph.CO].
[18] N. Kaiser, Clustering in real space and in redshift space, Monthly Notices of the Royal Astronomical Society **227**, 1 (1987), https://academic.oup.com/mnras/article-pdf/227/1/1/18522208/mnras227-0001.pdf.
[19] K. B. Fisher, O. Lahav, Y. Hoffman, D. Lynden-Bell, and S. Zaroubi, Wiener reconstruction of density, velocity and potential fields from all-sky galaxy redshift surveys,

MNRAS **272**, 885 (1995), arXiv:astro-ph/9406009 [astro-ph].

[20] Planck Collaboration, Y. Akrami, F. Arroja, M. Ashdown, J. Aumont, C. Baccigalupi, M. Ballardini, A. J. Banday, R. B. Barreiro, N. Bartolo, S. Basak, K. Benabed, J. P. Bernard, M. Bersanelli, P. Bielewicz, J. J. Bock, J. R. Bond, J. Borrill, F. R. Bouchet, F. Boulanger, M. Bucher, C. Burigana, R. C. Butler, E. Calabrese, J. F. Cardoso, J. Carron, A. Challinor, H. C. Chiang, L. P. L. Colombo, C. Combet, D. Contreras, B. P. Crill, F. Cuttaia, P. de Bernardis, G. de Zotti, J. Delabrouille, J. M. Delouis, E. Di Valentino, J. M. Diego, S. Donzelli, O. Doré, M. Douspis, A. Ducout, X. Dupac, S. Dusini, G. Efstathiou, F. Elsner, T. A. Enßlin, H. K. Eriksen, Y. Fantaye, J. Fergusson, R. Fernandez-Cobos, F. Finelli, F. Forastieri, M. Frailis, E. Franceschi, A. Frolov, S. Galeotta, S. Galli, K. Ganga, C. Gauthier, R. T. Génova-Santos, M. Gerbino, T. Ghosh, J. González-Nuevo, K. M. Górski, S. Gratton, A. Gruppuso, J. E. Gudmundsson, J. Hamann, W. Handley, F. K. Hansen, D. Herranz, E. Hivon, D. C. Hooper, Z. Huang, A. H. Jaffe, W. C. Jones, E. Keihänen, R. Keskitalo, K. Kiiveri, J. Kim, T. S. Kisner, N. Krachmalnicoff, M. Kunz, H. Kurki-Suonio, G. Lagache, J. M. Lamarre, A. Lasenby, M. Lattanzi, C. R. Lawrence, M. Le Jeune, J. Lesgourgues, F. Levrier, A. Lewis, M. Liguori, P. B. Lilje, V. Lindholm, M. López-Caniego, P. M. Lubin, Y. Z. Ma, J. F. Macías-Pérez, G. Maggio, D. Maino, N. Mandolesi, A. Mangilli, A. Marcos-Caballero, M. Maris, P. G. Martin, E. Martínez-González, S. Matarrese, N. Mauri, J. D. McEwen, P. D. Meerburg, P. R. Meinhold, A. Melchiorri, A. Mennella, M. Migliaccio, S. Mitra, M. A. Miville-Deschênes, D. Molinari, A. Moneti, L. Montier, G. Morgante, A. Moss, M. Münchmeyer, P. Natoli, H. U. Nørgaard-Nielsen, L. Pagano, D. Paoletti, B. Partridge, G. Patanchon, H. V. Peiris, F. Perrotta, V. Pettorino, F. Piacentini, L. Polastri, G. Polenta, J. L. Puget, J. P. Rachen, M. Reinecke, M. Remazeilles, A. Renzi, G. Rocha, C. Rosset, G. Roudier, J. A. Rubiño-Martín, B. Ruiz-Granados, L. Salvati, M. Sandri, M. Savelainen, D. Scott, E. P. S. Shellard, M. Shiraishi, C. Sirignano, G. Sirri, L. D. Spencer, R. Sunyaev, A. S. Suur-Uski, J. A. Tauber, D. Tavagnacco, M. Tenti, L. Toffolatti, M. Tomasi, T. Trombetti, J. Valiviita, B. Van Tent, P. Vielva, F. Villa, N. Vittorio, B. D. Wandelt, I. K. Wehus, S. D. M. White, A. Zacchei, J. P. Zibin, and A. Zonca, Planck 2018 results. X. Constraints on inflation, A&A **641**, A10 (2020), arXiv:1807.06211 [astro-ph.CO].

[21] N. Dalal, O. Dore, D. Huterer, and A. Shirokov, The imprints of primordial non-gaussianities on large-scale structure: scale dependent bias and abundance of virialized objects, Phys. Rev. D **77**, 123514 (2008), arXiv:0710.4560 [astro-ph].

[22] Y. Zhang, A. R. Pullen, and A. S. Maniyar, Joint analyses of 2D CMB lensing and 3D galaxy clustering in the spherical Fourier-Bessel basis, Phys. Rev. D **104**, 103523 (2021), arXiv:2110.00872 [astro-ph.CO].

[23] Planck Collaboration, Y. Akrami, F. Arroja, M. Ashdown, J. Aumont, C. Baccigalupi, M. Ballardini, A. J. Banday, R. B. Barreiro, N. Bartolo, S. Basak, K. Benabed, J. P. Bernard, M. Bersanelli, P. Bielewicz, J. R. Bond, J. Borrill, F. R. Bouchet, M. Bucher, C. Burigana, R. C. Butler, E. Calabrese, J. F. Cardoso, B. Casaponsa, A. Challinor, H. C. Chiang, L. P. L. Colombo, C. Combet, B. P. Crill, F. Cuttaia, P. de Bernardis, A. de Rosa, G. de Zotti, J. Delabrouille, J. M. Delouis, E. Di Valentino, J. M. Diego, O. Doré, M. Douspis, A. Ducout, X. Dupac, S. Dusini, G. Efstathiou, F. Elsner, T. A. Enßlin, H. K. Eriksen, Y. Fantaye, J. Fergusson, R. Fernandez-Cobos, F. Finelli, M. Frailis, A. A. Fraisse, E. Franceschi, A. Frolov, S. Galeotta, S. Galli, K. Ganga, R. T. Génova-Santos, M. Gerbino, J. González-Nuevo, K. M. Górski, S. Gratton, A. Gruppuso, J. E. Gudmundsson, J. Hamann, W. Handley, F. K. Hansen, D. Herranz, E. Hivon, Z. Huang, A. H. Jaffe, W. C. Jones, G. Jung, E. Keihänen, R. Keskitalo, K. Kiiveri, J. Kim, N. Krachmalnicoff, M. Kunz, H. Kurki-Suonio, J. M. Lamarre, A. Lasenby, M. Lattanzi, C. R. Lawrence, M. Le Jeune, F. Levrier, A. Lewis, M. Liguori, P. B. Lilje, V. Lindholm, M. López-Caniego, Y. Z. Ma, J. F. Macías-Pérez, G. Maggio, D. Maino, N. Mandolesi, A. Marcos-Caballero, M. Maris, P. G. Martin, E. Martínez-González, S. Matarrese, N. Mauri, J. D. McEwen, P. D. Meerburg, P. R. Meinhold, A. Melchiorri, A. Mennella, M. Migliaccio, M. A. Miville-Deschênes, D. Molinari, A. Moneti, L. Montier, G. Morgante, A. Moss, M. Münchmeyer, P. Natoli, F. Oppizzi, L. Pagano, D. Paoletti, B. Partridge, G. Patanchon, F. Perrotta, V. Pettorino, F. Piacentini, G. Polenta, J. L. Puget, J. P. Rachen, B. Racine, M. Reinecke, M. Remazeilles, A. Renzi, G. Rocha, J. A. Rubiño-Martín, B. Ruiz-Granados, L. Salvati, M. Savelainen, D. Scott, E. P. S. Shellard, M. Shiraishi, C. Sirignano, G. Sirri, K. Smith, L. D. Spencer, L. Stanco, R. Sunyaev, A. S. Suur-Uski, J. A. Tauber, D. Tavagnacco, M. Tenti, L. Toffolatti, M. Tomasi, T. Trombetti, J. Valiviita, B. Van Tent, P. Vielva, F. Villa, N. Vittorio, B. D. Wandelt, I. K. Wehus, A. Zacchei, and A. Zonca, Planck 2018 results. IX. Constraints on primordial non-Gaussianity, A&A **641**, A9 (2020), arXiv:1905.05697 [astro-ph.CO].

[24] https://github.com/JuliaApproximation/FastGaussQuadrature.jl.

[25] D. N. Limber, The Analysis of Counts of the Extragalactic Nebulae in Terms of a Fluctuating Density Field. II., ApJ **119**, 655 (1954).

[26] M. LoVerde and N. Afshordi, Extended Limber approximation, Phys. Rev. D **78**, 123506 (2008), arXiv:0809.5112 [astro-ph].